

Rapid pseudo-H&E imaging using a fluorescence-inbuilt optical coherence microscopic imaging system

SEY-EN LIN,^{1,2}  DONG-YO JHENG,¹ KUANG-YU HSU,¹ YUN-RU LIU,³ WEI-HSIANG HUANG,⁴ HSIANG-CHIEH LEE,^{5,6}  AND CHIEN-CHUNG TSAI^{1,*} 

¹*AcuSolutions Inc., 3F., No. 2, Ln. 263, Chongyang Rd., Nangang Dist., Taipei, Taiwan*

²*Department of Anatomic Pathology, New Taipei Municipal Tucheng Hospital (Built and operated by Chang Gung Medical Foundation), New Taipei City, Taiwan*

³*Joint Biobank, Office of Human Research, Taipei Medical University, Taipei, Taiwan*

⁴*Graduate Institute of Molecular and Comparative Pathobiology, School of Veterinary Medicine, National Taiwan University, Taipei, Taiwan*

⁵*Graduate Institute of Photonics and Optoelectronics, National Taiwan University, Taipei, Taiwan*

⁶*Department of Electrical Engineering, National Taiwan University, Taipei, Taiwan*

**cctsai@acusolutions.com*

Abstract: A technique using Linnik-based optical coherence microscopy (OCM), with built-in fluorescence microscopy (FM), is demonstrated here to describe cellular-level morphology for fresh porcine and biobank tissue specimens. The proposed method utilizes color-coding to generate digital pseudo-H&E (p-H&E) images. Using the same camera, colocalized FM images are merged with corresponding morphological OCM images using a 24-bit RGB composition process to generate position-matched p-H&E images. From receipt of dissected fresh tissue piece to generation of stitched images, the total processing time is <15 min for a 1-cm² specimen, which is on average two times faster than frozen-section H&E process for fatty or water-rich fresh tissue specimens. This technique was successfully used to scan human and animal fresh tissue pieces, demonstrating its applicability for both biobank and veterinary purposes. We provide an in-depth comparison between p-H&E and human frozen-section H&E images acquired from the same metastatic sentinel lymph node slice (~10 μm thick), and show the differences, like elastic fibers of a tiny blood vessel and cytoplasm of tumor cells. This optical sectioning technique provides histopathologists with a convenient assessment method that outputs large-field H&E-like images of fresh tissue pieces without requiring any physical embedment.

© 2021 Optical Society of America under the terms of the [OSA Open Access Publishing Agreement](#)

1. Introduction

Optical coherence tomography (OCT) evolved from low-coherence white-light interferometry [1]. In clinical practice, optical-path-length concept of OCT was first used for *in vivo* ocular measurements [2]. OCT technology [3], such as frequency-domain OCT [4], has been used to acquire *in vivo* tomographic retinal images. Owing to its optical sectioning property, OCT is applied in oncology [5] for rapid intraoperative diagnosis. Although spectral-domain OCT [6] can be used for rapid diagnosis, it lacks the required lateral resolution and nuclear information for histological diagnosis. Full-field OCT (FF-OCT) [7], a type of time-domain OCT, reconstructs axially stacked *en-face* optical coherence microscopy (OCM) [8] images to generate a series of continuous adjacent tomographic images acquired commonly using a broadband tungsten halogen lamp [9], high numerical aperture objective lens, and CCD/CMOS camera; FF-OCT can capture the cellular-level morphological images of biological tissues [10,11] at submicron spatial resolution. FF-OCT has been adopted in pathological studies to investigate the feasibility

of skipping the use of frozen sections for rapid diagnosis [12] by using large-field *en-face* images [13,14]. However, low nucleus reflectance remains a drawback of such histopathological assessment, which results in a high false-positive rate ($\sim 23\%$) [13]. To provide more nuclear information, dynamic FF-OCT (d-FF-OCT or so-called dynamic cell imaging [DCI]) was proposed [15]. In a recent study [16], the false-positive rate of FF-OCT combined with DCI significantly reduced the false-positive rate ($\sim 4\%$); however, this method did not enhance nucleus reflectance [17]. In practice, pathologists utilize knowledge regarding both cytoplasmic morphology and cellular nucleus properties when diagnosing diseases. Typically, cell nuclei in biological tissues, such as epithelial cells, exhibit poor reflection characteristics under OCM owing to the homogeneous distribution of DNAs and RNAs [18,19]. Therefore, other techniques are required to examine nuclei effectively. Similar to OCM (which is based on reflectance), only confocal reflectance microscopy part of Vivascope 2500 of Caliber I.D. cannot reveal detailed cellular properties of nuclei [20] by reflectance. So, tissue morphology images alone are insufficient for pathologists to diagnose a disease. Fluorescence microscopy (FM) is a direct method for imaging organelles, like nuclei, at shallow tissue depths; however, strong background noise causes considerable disturbance for image contrast. Confocal fluorescence microscopy using laser-scanning excitation can significantly decrease background noise, and it has been applied for imaging the nucleus by using acridine orange (AO) [21], like HistologTM of Saman Tree. However, only nuclear information is also insufficient for histopathological diagnosis.

A study conducted in 2010 performed fluorescence imaging combined with OCT to elucidate both molecular and morphological information at a lower lateral resolution [22]. Structured illumination microscopy (SIM) is a substitutional method used for obtaining a background-noise-eliminated fluorescence image with wide-field illumination through the use of a halogen lamp or LED. On the basis of the aforementioned method, a dual-modality system combining OCM with submicron SIM-based FM [23] was proposed for merging tissue morphologies with the fluorescing cell population at a higher lateral resolution. In addition, this method was applied to fluorescent nuclei in a fresh tissue piece [24]. However, this method produces a gray morphological image with merged green, fluorescent nuclei on a black background; pathologists encounter difficulty in establishing a diagnosis based on this image because they are familiar with bright-field H&E images and require significant training in evaluating such an image.

The first pseudo-H&E (p-H&E) image [25] of a dissected fresh tissue specimen was generated through a combination of confocal reflectance and confocal fluorescence microscopy by using AO [26] to stain nuclei, like Vivascope 2500 of Caliber I.D. (scan speed: $0.9 \text{ cm}^2/\text{min}$). In 2014, AO-stained dissected fresh tissue specimen was imaged through nonlinear microscopy (NLM) with a scan speed of $0.12 \text{ cm}^2/\text{min}$, and a virtual H&E color-coding method that produced color maps resembling typical H&E images was proposed to replace frozen sections for H&E staining [27]. The tunable Ti:sapphire laser allows the use of a wide range of dyes because the output wavelength can be tuned. However, the use of the femtosecond mode-locked Ti:sapphire laser to generate nonlinear effects in fresh tissue pieces is limited by cost, reliability, robustness, and footprint. Recently, the NLM light source has progressively used the unamplified (low-power) femtosecond Yb fiber laser because of its compactness, high reliability, and cost-effectiveness; however, an additional cytoplasm-enhancing stain such as sulforhodamine 101 (initially for observing neural morphology) is required for coding eosin color [28]. For realizing label-free, optical H&E-like sectioning, stimulated Raman scattering (SRS) microscopy was proposed [29]. However, SRS microscopy is limited by a scan speed of approximately $0.5 \text{ mm}^2/\text{min}$, which is appropriate for detecting small structures such as brain tumors [30]. In addition, SRS using a tunable laser has the same light source problems as NLM. To eliminate the use of a laser source, dual-component stained SIM with DRAQ5 and eosin was proposed and applied for evaluating an intact fresh kidney biopsy tissue specimen; however, a blurred image was obtained (similar to the normal glomerulus) because of the background noise of the eosin stain

[31]. Microscopy with ultraviolet surface excitation (MUSE), which is generally used for the surface scan of formalin-fixed tissue, was applied on fresh tissue pieces by using ATTO 655 NHS ester (cytoplasmic stain) and SYBR Gold (nucleus stain) [32], with a scan speed of $0.2 \text{ cm}^2/\text{min}$; however, MUSE using 285-nm excitation UV light still showed a tissue penetration of less than $25 \text{ }\mu\text{m}$ [33]. An open-top light-sheet (OTLS) [34] microscope showed a high scan speed of $1.5 \text{ cm}^2/\text{min}$ when the same fluorescent dyes, namely ATTO 655 NHS ester and SYBR Gold, were used. The image processing time (15 min for 1-cm^2 image data) was fast, but image quality was not sufficient for high-resolution assessment. Each of the aforementioned imaging modalities has its own advantages and limitations [35].

In this study, we proposed a method that performs optical p-H&E sectioning through fluorescence-inbuilt OCM (f-OCM) [36]; this method was applied to a fresh porcine cerebrum tissue piece. The proposed approach can generate corresponding p-H&E images after a step-by-step *en-face* scan in real time [37] for further stitching a large-field p-H&E image. The quality of the image of the fresh porcine kidney piece acquired using f-OCM was higher than that acquired using optical sectioning SIM [31]; our p-H&E image provides various morphological details of the cellular structure. Moreover, fresh porcine and human (provided by a biobank) tissue pieces were used to evaluate the image quality of this system. Finally, a comprehensive comparison of p-H&E and traditional H&E images obtained from the scans of the same $10\text{-}\mu\text{m}$ -thick frozen-sectioned metastatic sentinel lymph node (SLN) slice was performed, and the images showed high correlation and similarity. f-OCM with a scan speed of $0.25 \text{ cm}^2/\text{min}$ can be used to assess fresh, small-sized pieces, such as a brain tumor or breast core-needle biopsy tissue, for surgical evaluation.

2. Experimental setup and imaging methods

Figure 1(a) shows the schematic of the f-OCM setup, which includes OCM and FM. The p-H&E images combine cytoplasmic morphology and nuclei-related details obtained from OCM and FM, respectively. Figure 1(b) shows the movable device hardware (AcuOnPath, AcuSolutions Inc.) including the scan machine and control box, which were designed for research use and preclinical testing. In this system, a broadband light source serves as a low-coherence light source, and the measured spectrum and measured interferometric signal of which are shown in Fig. 1(c) and 1(d), respectively. In contrast to traditional FF-OCT, which operates at near-infrared wavelengths, the OCM part of the f-OCM system utilizes a visible-range broadband light source to obtain high lateral and axial resolutions for facilitating the observation of fine cellular features. OCM detects only ultra-weak signals from nucleus reflection. To address this issue, an FM excitation path was incorporated into the sample arm of the OCM structure to enable f-OCM. In contrast to traditional dual-modality FM and FF-OCM [23] that merge two spectral light sources before a beam splitter, our method implementing FM can reflect and reject most of the excitation light using the same dichroic mirror, resulting in decreased loss of intensity from nuclei-emitted signals because signals do not have to pass through the beamsplitter twice. Table 1 shows theoretical and measured resolutions along axial and lateral directions for OCM, FM, and pixel. Here, the pixel resolution along the lateral dimension is determined as the equivalent lateral size of the focal plane of a sample projected from the single pixel of CMOS camera. It is the capability of spatial division restricted by CMOS camera pixel size. Data of Table 1 will be brought out in Secs. 2.1 and 2.2.

2.1. OCM

A collimated beam from the broadband light (BL) source (Thorlabs, #SOLIS-2C) was used as the low-coherence light source (Fig. 1(a)), with the spectral spike at 450 nm blocked by a long-pass filter. The output spectrum is shown in Fig. 1(c), where the maximal incident power onto the specimen (S) was approximately 5 mW. The output of BL light beam was divided into reference

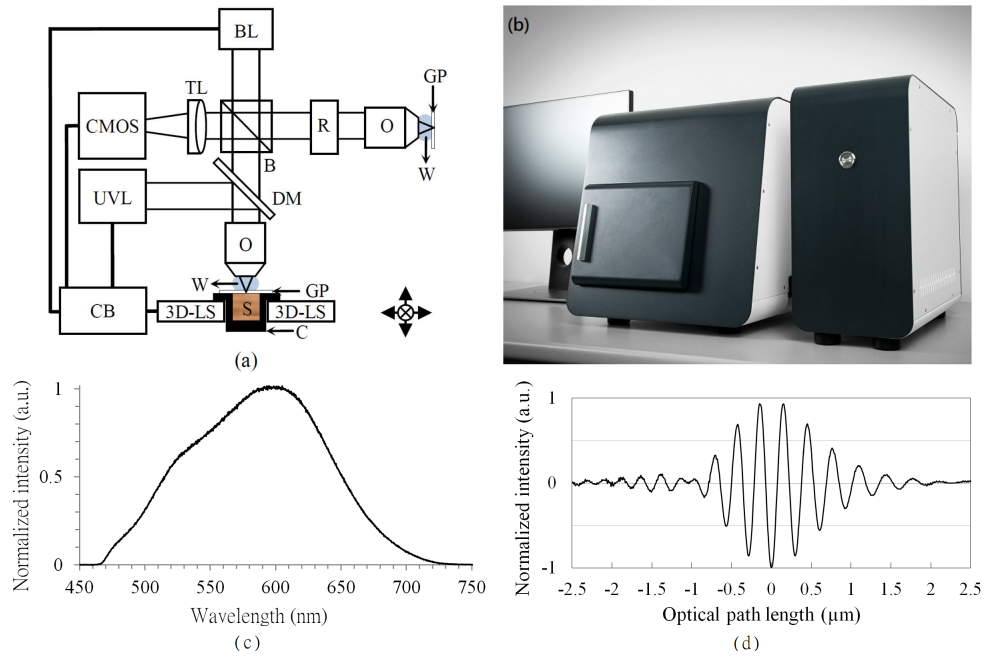


Fig. 1. (a) Schematic of the f-OCM experimental setup. BL: broadband light; UVL: ultraviolet light; DM: dichroic mirror; C: container; B: beamsplitter; R: retarder; O: objective; W: water; GP: glass plate; S: specimen; 3D-LS: 3D linear stage; CB: control box; TL: tube lens; CMOS: mono complementary metal-oxide semiconductor camera. (b) Front view of the f-OCM device (AcuOnPath), including the scan machine (left, approximately $40 \times 40 \times 40 \text{ cm}^3$) and the control box (right, approximately $40 \times 20 \times 40 \text{ cm}^3$). (c) Output spectrum and (d) the corresponding interferometric signal of BL.

Table 1. Theoretical and measured resolutions of R_a (axial) and R_l (lateral) for OCM, FM, and pixel.

Resolution (μm)	OCM	FM	Pixel
Theoretical R_a	0.60	2.19	—
Theoretical R_l	0.45	0.38	0.37
Measured R_a	0.81	3.03	—
Measured R_l	0.60	0.45	0.38

and sample beams by a 50:50 beamsplitter (B). Two same objective lenses (O) (Nikon, NA: 0.8, water dipping) were used in reference and sample arms. The central wavelength λ_0 and spectral bandwidth (FWHM) $\Delta\lambda$ measured in the plane of the CMOS camera were 590 and 138 nm, respectively, theoretically providing a coherence length (coherence gate in tissue [$n_{\text{tissue}} = \sim 1.4$, normal soft tissue] [38] equal to $0.44\lambda_0^2/n_{\text{tissue}}\Delta\lambda$ [18]) of 0.79 μm . The theoretical depth of focus (confocal gate in tissue equal to $2\lambda_0 n_{\text{tissue}}/\text{NA}^2$ [18]) was 2.58 μm (NA: 0.8).

The reflectance between the N-BK7 glass plate (GP, thickness: 500 μm) and air in the reference arm was approximately 4%, which was appropriate for obtaining satisfactory interference efficiency for general fresh tissues. For the sample beam, all optical components are identical to those used in the reference arm. The specimen (S) was placed into a container (C) on a 3D linear stage (3D-LS; Thorlabs, #MLS203-1/MZS500-E), which included a biaxial DC-servo linear stage and a z-axial piezoelectric stage. Both reference and sample beams were reflected,

combined, and then projected onto a monochrome CMOS camera through a tube lens (TL; Thorlabs, #TL200-CLS2, effective focal length: 20 cm). Raw images were then captured and processed. As shown in Fig. 1(a), a tiny displacement (equivalent to five interferometric carrier fringes, approximately 1.07 μm in tissue) along the z-axial direction (controlled by the 3D-LS) generated one *en-face* OCM image.

To enable focal and coherent planes be coplanar, the retarder (R) was adjusted through the projected images of the CMOS camera. Considering both confocal-gate (depth-of-focus) and coherent-gate (coherent-length) effects, the theoretical axial resolution R_a in the tissue, equal to $[(0.44\lambda_0^2/n_{\text{tissue}}\Delta\lambda)^{-1} + (2\lambda_0 n_{\text{tissue}}/NA^2)^{-1}]^{-1}$ [18], was approximately 0.60 μm ; however, the measured R_a in the tissue based on the envelope FWHM of interferometric carrier wave shown in Fig. 1(d) was approximately 0.81 μm . By contrast, the estimated theoretical lateral resolution R_l in the tissue was 0.45 μm (resolution power equal to $0.61\lambda_0/NA$), whereas the measured R_l determined using a knife-edge test [18] was 0.60 μm near the surface of the GP. These measurements were due to the equivalent coating bandwidth of all optical components and the total effect of dispersion on light transmitted by GPs in both arms. On the basis of the imaging properties of O and TL, the equivalent pixel lateral resolution R_l was determined to be 0.37 μm , whereas the real pixel lateral resolution R_l measured according to the x-axial position of 3D-LS was 0.38 μm . In AcuOnPath, the field of view (FOV) calculated from the CMOS camera with 2390 (width) \times 1936 (height) pixels was 908 μm (width) \times 736 μm (height) in the tissue.

The CMOS camera has a maximum frame rate of approximately 160 frame/s. Raw images collected within 1 s were averaged to generate 20 new images with a higher SNR. These images enabled five reconstructed OCM images using a four-step phase shifting algorithm (phase: 0°, 90°, 180°, and 270°) [18]. Then, these five continuous single-wave images were averaged again to create a final high-quality *en-face* OCM image. OCM had an optimized depth scanning speed of 1.07 $\mu\text{m/s}$ for an *en-face* OCM image, depending on the refractive index of the fresh tissue being tested. In other words, one OCM *en-face* image was output by averaging 20 raw images. The duration of each *en-face* OCM scan performed using the large-field stitched mode was set as 1 s, where the integral carrier fringe number was 5 and the equivalent scan depth was 1.07 μm in the tissue.

2.2. FM

As shown in Fig. 1(a), another collimated beam of UV light ($\lambda_0 = 385 \text{ nm}$; Thorlabs, #SOLIS-385C) was used to excite Hoechst 33342 to allow nuclei imaging. The central wavelength λ_0 of the emission spectrum of Hoechst 33342 was approximately 500 nm. This excitation beam was reflected by a long-pass dichroic mirror (DM; Semrock, #LP02-407RU-25) before being focused onto S through O. The incident excitation UV light focused onto the sample was approximately 15 mW. Fluorescent light emitted from the nuclei of S was collected by O. Most residual excitation light reflected and scattered by S was blocked by the dichroic mirror, and the emitted fluorescence light was projected onto the CMOS camera through TL.

The focal plane is adjusted to penetrate deeper into the sample. The theoretical R_l (0.38 μm , equal to $0.61\lambda_0/NA$, where λ_0 is 500 nm) of FM, which is caused by the decreased dispersion of single transmission trip, is better than that of OCM, for which the measured R_l was 0.45 μm . However, the R_a of FM was lower (depending on the depth of field) than that of OCM. The theoretical (depth of focus, equal to $2\lambda_0 n_{\text{tissue}}/NA^2$, where λ_0 is 500 nm) and measured (by measuring FWHM of 50- μm -diameter fluorescent nanobeads) R_a values were 2.19 and 3.03 μm , respectively. In addition, to obtain the highest frame rate for acquiring fluorescent images, the exposure time was set as 0.6 ms, which was consistent with the 160 frame/s of the CMOS camera. After completing the OCM process, eight FM images were collected and averaged to form a single high-quality image. For the CMOS camera, a high-quality image obtained through frame averaging was better than that obtained using longer integration time because switching

integration time between OCM and FM modes require additional time that can affect the scan speed of a large-field stitched image. Finally, the output frame rate of the CMOS camera is 20 frame/s for FM, identical to that for OCM.

In contrast to confocal microscopy, this wide-field FM has a certain amount of background noise resulting from excited back-scattering fluorescence, which affects the contrast of nucleus images. Here, acquired FM images were obtained after background subtraction to enhance the contrast. A background subtraction algorithm [39] was used to enhance the nucleus image contrast, where the parameter of rolling ball radius was set to 16 before magnifying the subtracted nucleus image.

2.3. P-H&E, the composite image of OCM and FM

A simple color-coding method similar to that proposed by Gareau *et al.* [25] is shown in Fig. 2. The 8-bit gray OCM images were converted into 24-bit RGB images with dark-green color and black backgrounds; 8-bit gray FM images were converted into 24-bit RGB images with yellow-green color and black backgrounds. Subsequently, these two transformed images were combined (summed) and inverted to create 24-bit RGB format p-H&E images. Because of the tissue inhomogeneous property, induced nuclear background noise needs to be substantially eliminated from the image of FM for obtaining a composite high-quality p-H&E image. The FM image needs to be processed after background subtraction before the color-coding process. Otherwise, the obtained composite image would be blurred.

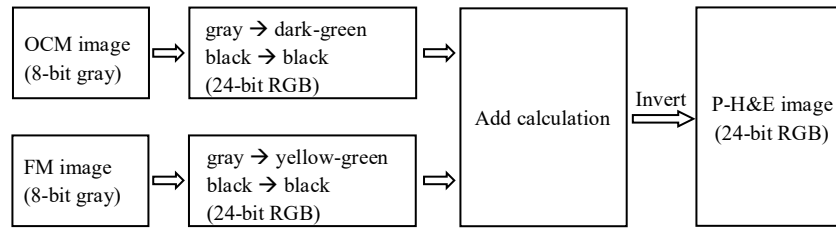


Fig. 2. Flowchart of the color-coding process for producing p-H&E images.

(R, G, B) is the 24-bit RGB gain set of an 8-bit gray-level image, where R , G , and B are all between 0 and 1. The color-coding process is demonstrated for OCM and FM images in Fig. 3: a gray-level scale cytoplasmic OCM image $I_{Cy}(x_i, y_j)$ (Fig. 3(a)) was multiplied by $(R, G, B)_{Cy} = (1, 0, 0)$ to obtain a red-level image with a black background, and a gray-level nucleus FM image $I_{Nu}(x_i, y_j)$ (Fig. 3(b)) was multiplied by $(R, G, B)_{Nu} = (0, 1, 0)$ to obtain a green-level image with a black background. Subsequently, OCM and FM processing paths were combined to produce a red-and-green image with a black background (Fig. 3(c)).

Typically, $(0, 0.2, 0) \leq (R, G, B)_{Cy} \leq (0.2, 1, 0.2)$ for $I_{Cy}(x_i, y_j)$ combined with $(0.5, 0.7, 0) \leq (R, G, B)_{Nu} \leq (1, 1, 0.3)$ for $I_{Nu}(x_i, y_j)$ had a yellow-and-deep-green color scheme with a black background. After being inverted, it became a pink-and-blue-violet color scheme with a white background, which is traditionally associated with H&E images [24]. $(R, G, B)_{Cy}$ and $(R, G, B)_{Nu}$ were respectively fine-tuned to be $(0, 0.60, 0.05)$ and $(0.80, 1, 0.21)$ by a histopathologist through comparison of numerous f-OCM scan images with many formalin-fixed paraffin-embedded H&E images of original tissues. These two gain sets were used to output Fig. 3(d). Figure 3 represents the images of the fresh porcine cerebrum tissue piece scanned using the f-OCM instrument after soaking in AcuSolutions pretreatment medium (PM) #2 for 5 min following process I shown in Fig. 4. The images reveal the details of neural and glial cells within the cerebral cortex, with nuclei clearly observed.

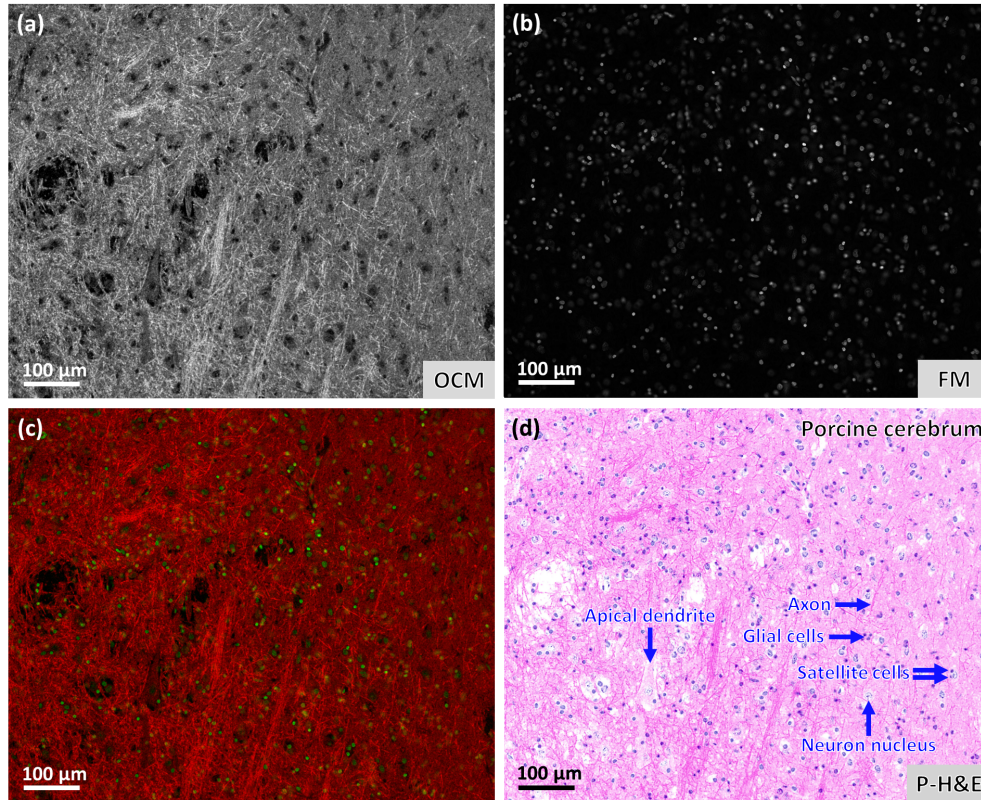


Fig. 3. (a)–(d) Co-localized images of the fresh porcine cerebrum tissue piece: (a) OCM morphological image of the cytoplasmic structure; (b) co-located FM image highlighting the positions of nuclei; (c) red-and-green OCM/FM composite image; and (d) traditional pink-and-blue-violet color scheme with structural features labeled. All images correspond to a tissue depth of 25 μm with the same FOV (908 μm [W] \times 736 μm [H]).

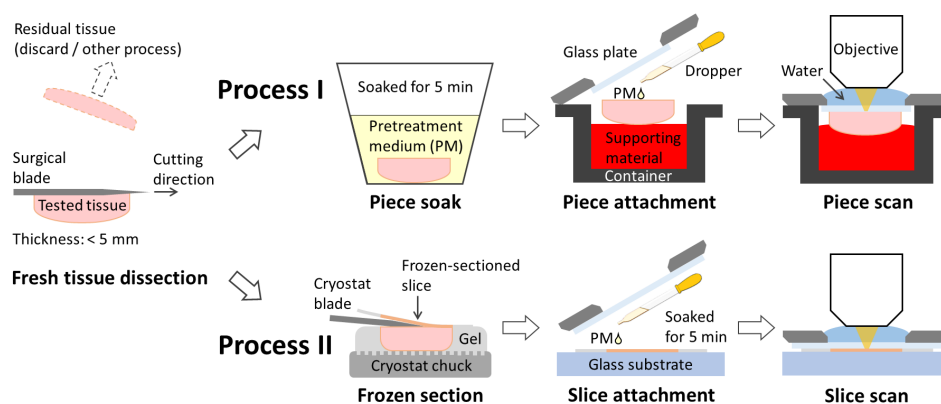


Fig. 4. Two processing methods of fresh tissue samples after dissection by using a surgical blade. Process I shows the material preparation of fresh tissue pieces for producing p-H&E images. Process II shows the material preparation of frozen-sectioned slices for image validation purposes, and comprehensive comparison between p-H&E and H&E-stained images.

3. Experimental results: p-H&E images of fresh tissue pieces and frozen-sectioned slice

As shown in Fig. 4, two additional processes were introduced for fresh tissue specimens obtained after dissection by using a surgical blade. In process I, the tested tissue specimen was soaked in AcuSolutions pretreatment medium (PM) #1 or #2 for 5 min, where PMs #1 and #2 will be described later. Subsequently, the soaked tissue specimen was carefully placed on the supporting material (soft sponge) of the container. The acceptable tissue size was less than 2 cm (W) \times 2 cm (H) \times 0.5 cm (T); thus, p-H&E imaging can be applied on thick tissue specimens. Then, a cover glass was carefully pressed and attached to the soaked tissue specimen after dropping PM #1 or #2 (using the same PM of previous soak) on the surface of the soaked tissue specimen. Finally, this container was positioned inside the AcuOnPath instrument for p-H&E scanned. In process II, the tested tissue surrounded by cryostat gel was placed on the aluminum chuck and then cooled down to -20°C for obtaining a frozen-sectioned slice. Then, a 10- μm -thick slice was produced and affixed on the 1-mm-thick glass substrate (GS, or glass slide). The specimen prepared using process II was obtained only for performing a comprehensive co-localized comparison between p-H&E and frozen-sectioned H&E images for image validation. The frozen-sectioned slice was completely submerged in PM #2 for 5 min. Then, a glass plate was slightly placed on the soaked frozen-sectioned slice and glass substrate for further p-H&E scanning in AcuOnPath.

The concentration of fluorescent dyes in PM #1 was 50 $\mu\text{g}/\text{mL}$ (dissolved in $1\times$ PBS); this concentration exerted a minimal effect on the section in case the soaked tissue specimen was required for follow-up RNA extraction at the biobank. The concentration of fluorescent dyes in PM #2 was 33 $\mu\text{g}/\text{mL}$; the dyes were dissolved in a glycol-compound buffer solution with 1.3% formaldehyde. Similarly, this process did not preclude the soaked tissue specimen from being used in further protocols, such as DNA extraction, immunohistochemistry (IHC), or formalin-fixed paraffin-embedded H&E staining.

The AcuOnPath instrument produces p-H&E images by stitching multiple side-by-side fields at a depth beneath surface of the fresh tissue specimen. Through the stitching method, a large-field p-H&E image of the dissected fresh tissue specimen was obtained, as indicated from the snapshot image of the real fresh porcine kidney tissue specimen in the container, where the scanned field could be cropped using our in-house developed AcuViewer interface. The scanned p-H&E images of the flatly dissected tissue specimens collected from different fresh porcine organs could be obtained for examining various histological structures. In addition, two thyroid and two fresh breast tissue specimens were tested before storing them in -80°C refrigerator for biobank application. Finally, to compare p-H&E images with traditional H&E images, a frozen-sectioned slice with a thickness of 10 μm was prepared and scanned using f-OCM. After acquiring the p-H&E image, this frozen-sectioned slice was stained with H&E dyes to validate the p-H&E imaging method.

3.1. Large-field p-H&E image of the normal fresh tissue piece

According to process I shown in Fig. 4(a) dissected fresh porcine kidney specimen was soaked in PM #2 for 5 min and then directly placed into a container for obtaining a large-field p-H&E image; the top-view snapshot of the container is shown in the top-right inset of Fig. 5(a). The cropped rectangular region (small green box) with 7×7 FOVs in the top-view snapshot of the container localized the real position of the stitched large-field p-H&E image shown in Fig. 5(a) (large green box) for the fresh tissue piece. The cropped area in the top-view snapshot of the container was limited by the window size of the glass plate ($2\times 2\text{ cm}^2$). Because of the degradation of the intact tissue specimen, many glomeruli in the fresh porcine kidney specimen were easily dropped after being cut. Figure 5(b) and 5(c) respectively shows the low- and high-magnified images from the red and blue boxes of Fig. 5(a). Figure 5(b) shows the low-resolution image of glomeruli and renal tubules from the red box of Fig. 5(a). Furthermore, Fig. 5(c) magnifies a single glomerulus

and its structure in detail from the blue box of Fig. 5(a). In Fig. 5(c), basic structures in the glomerulus and renal tubule of the normal porcine kidney [40], such as Bowman's capsule, parietal epithelial cells, capillary loop, red blood cells (typically in the hollow position of the capillary loop), and basement membrane, are distinctly observed. The full-size scan of this dissected fresh porcine kidney specimen could be selectively cropped using the AcuViewer interface.

3.2. Normal fresh tissue pieces of animal organs

The p-H&E images of six fresh porcine organs (lymph node, liver, skeletal muscle, salivary gland, lung, and esophagus) are presented in Figs. 6 and 7. Each organ was obtained through slaughter, with the organs transported at a temperature of 4°C in 12 h. Before performing f-OCM scans, each fresh porcine tissue specimen was soaked in PM #2 for 5 min following process I shown in Fig. 4. Figures 6(b), 6(d), 6(f), 7(b), 7(d), and 7(f) represent blue-bounded regions shown in Figs. 6(a), 6(c), 6(e), 7(a), 7(c), and 7(e) respectively, magnified by a factor of 2.

Figure 6(a) shows the p-H&E image of lymph nodes, revealing the population of nuclei, which was similar to the morphological property of tissue inflammation described in Fig. 6(b) in detail. In Fig. 6(b), the reticular fiber [41] could easily be observed because of the strong reflection of OCM; however, its observation through H&E staining appeared to be difficult [42]. In Fig. 6(c), showing the liver, the cell border between two adjacent hepatocytes could be readily identified, and the central vein and sinusoid [43] were well spaced, as shown in Fig. 6(d) in detail. In addition, as shown in Fig. 6(d), some hepatocytes were already autolytic and degraded. Figure 6(e) demonstrates the high spatial resolution of images by resolving the striations of muscular sarcomeres from the skeletal muscle.

Typically, the A-bands of the porcine skeletal muscle are fixed, with the measured sarcomere length representing the summation of A- and I-bands [44] at 2.2 μm . As shown in Fig. 6(f), the average sarcomere length was estimated to be 2.3 μm . Compared with alternative techniques used for imaging skeletal striations [45,46], including confocal and nonlinear microscopy, our method provides a convenient approach based on H&E-like images. In addition, the distributed heterochromatin of the single nucleus was discriminated. As shown in Fig. 7(a), the aggregations of mucous acini, serous acini, and sectioned intralobular ducts [47] were well arranged and are further indicated in Fig. 7(b), with the salivary gland showing similar signs of degradation as the liver, as shown in Fig. 6(d). Figure 7(b) reveals the proximity of intralobular ducts to the arteriole. Figure 7(c) shows the balloon-like structure in the p-H&E image of the lung [48], and the magnified image (Fig. 7(d)) represents the optically sectioned contour of the alveoli and arteriole clearly. Figure 7(e) shows the squamous epithelium and lamina propria regions of the mucosa of the esophagus tissue distinguished by a basal layer [49], and Fig. 7(f) describes the regions in detail. To obtain high-quality p-H&E images of fresh lung and esophagus specimens, the cutting flatness of the attached side and soft attachment is crucial. A high-sharpness (small bevel angle) surgical blade can help improve the cutting flatness.

3.3. Biobank-provided thyroid and breast tissue pieces

Two human intraoperative fresh thyroid tissue specimens (one specimen was normal and the other one was cancerous) were prepared for scanning following process I (soaked in PM #1 for 5 min) shown in Fig. 4. These specimens were then placed in a freezer at -80°C for biobank storage. The normal and cancerous tissue specimens of the thyroid were scanned using the AcuOnPath system, producing p-H&E images shown in Fig. 8(a) and (c), respectively. Subsequently, both original tissue pieces were frozen and sectioned as 4- μm -thick slices to acquire traditional H&E-stained images for comparison, as shown in Fig. 8(b) and (d). In Fig. 8(a) and (b), characteristic follicles that comprise the ultrastructure of the thyroid gland are easily identifiable. The abnormal structures of tumor-invaded tissue regions (Fig. 8(c) and (d)) are enclosed by brown lines. In

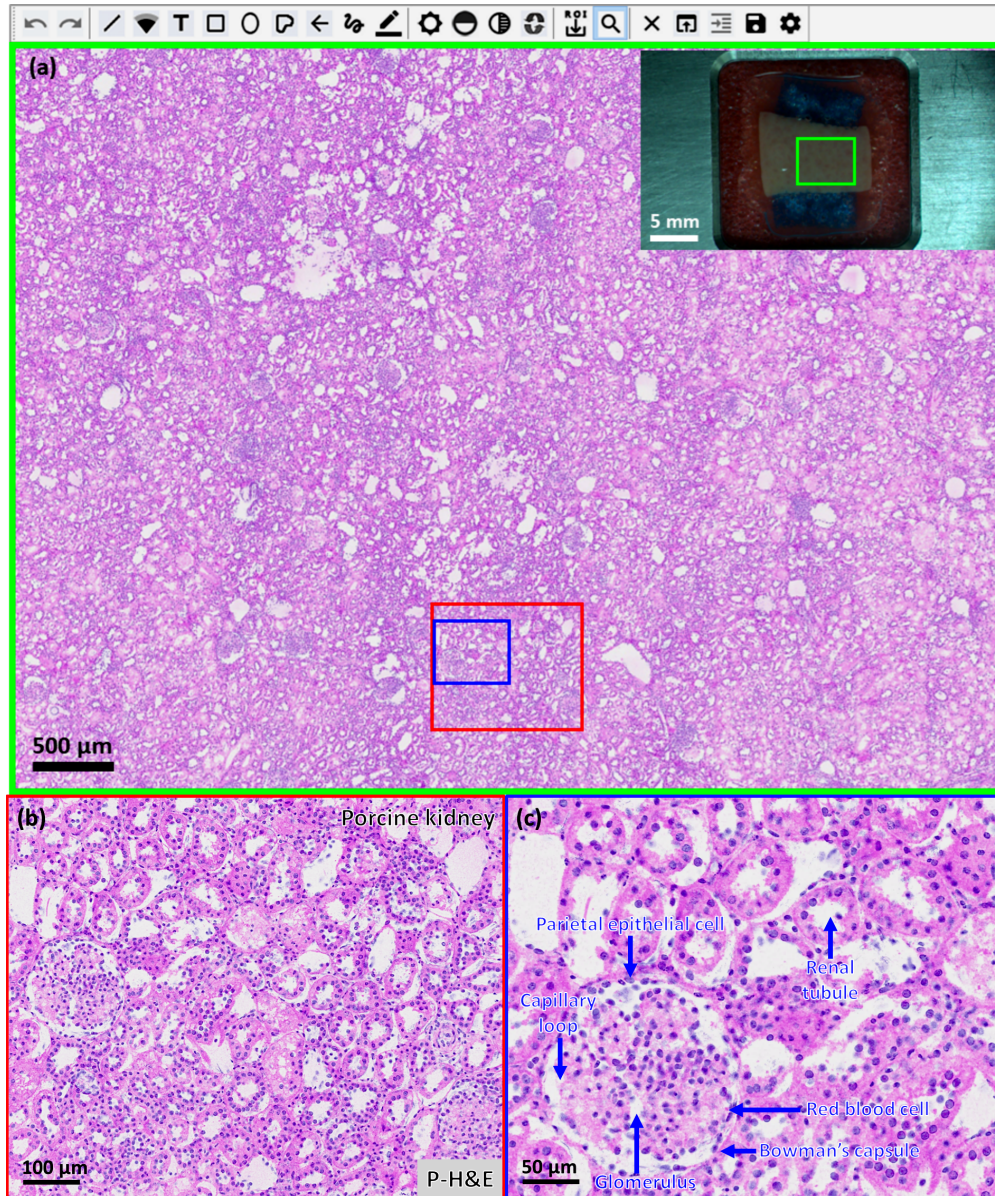


Fig. 5. (a) A large-field p-H&E image (inside large green box of AcuViewer interface) indicated by a navigator (top-right inset figure) with a top-view snapshot of the fresh porcine tissue piece in the container were scanned at a depth of 25 μm. The stitched size of the cropped small green box region is $6.1 \times 4.9 \text{ mm}^2$. (b) and (c) Low- and high-magnified images from red and blue boxes of (a), where the FOVs were $908 \text{ μm (W)} \times 736 \text{ μm (H)}$ and $454 \text{ μm (W)} \times 368 \text{ μm (H)}$, respectively.

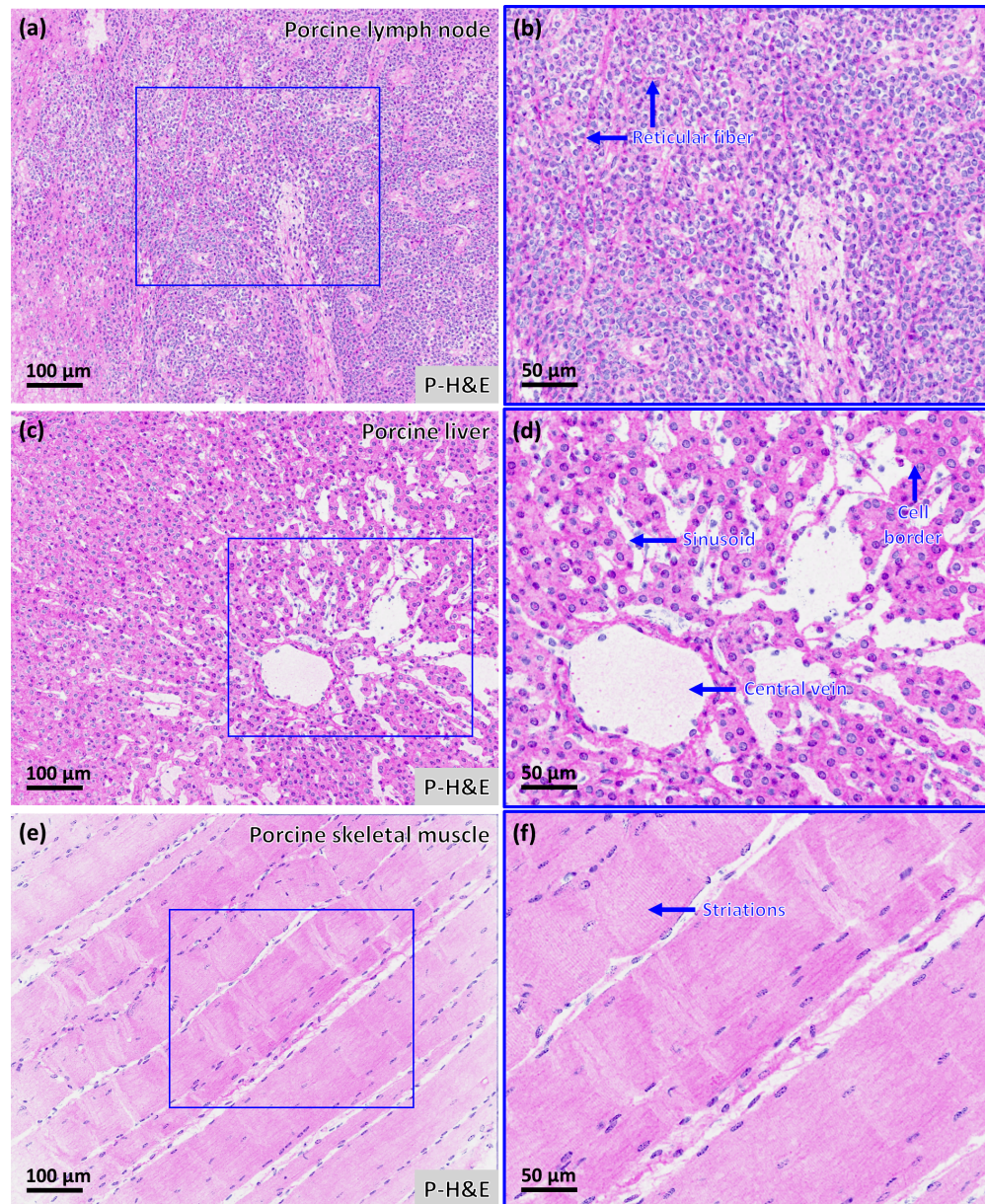


Fig. 6. P-H&E images of fresh porcine tissue pieces: (a) and (b) lymph node, (c) and (d) liver, and (e) and (f) skeletal muscle. The FOV of images (b), (d), and (f) was 454 μm (W) × 368 μm (H), corresponding to a quarter of the area shown in images (a), (c), and (e), respectively. All images were scanned at a depth of 25 μm.

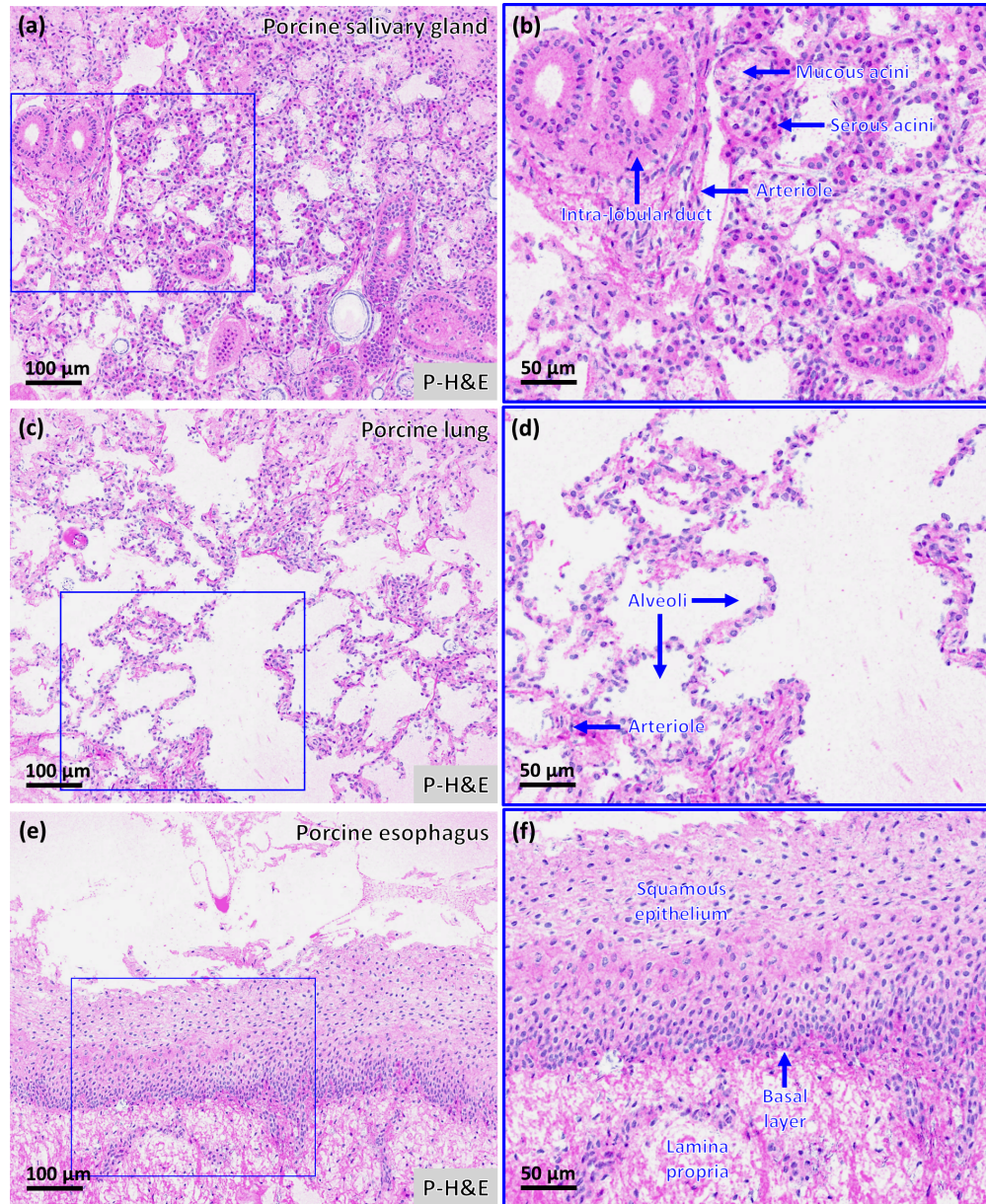


Fig. 7. P-H&E images of fresh porcine tissue pieces: (a) and (b) salivary gland, (c) and (d) lung, and (e) and (f) esophagus. The FOV of images (b), (d), and (f) was 454 μm (W) × 368 μm (H), corresponding to a quarter of the area shown in images (a), (c), and (e), respectively. All the images were scanned at a depth of 25 μm.

this case, it is capable to determine the area percentage of tumor for tissue quality check before warehouse entry. However, the boundary seems much less clear in the p-H&E image. It may be due to tissue over press onto the glass plate (see Fig. 4), which is easy to induce blur morphology for boundary identification. In addition, two intraoperative fresh breast tissue specimens, of which one was normal and the other cancerous, were prepared for scanning. Similar to the comparison of Fig. 8(a) and (c), Fig. 8(e) and (g) shows the p-H&E images of the normal and cancerous breast tissue specimens acquired using this system. Figure 8(f) and (h) shows the corresponding frozen H&E images of the 4- μ m-thick slice obtained from the original tissue specimens in Fig. 8(e) and (g). In Fig. 8(e), the morphology of adipocytes is more complete than that in Fig. 8(f) because the fatty tissue easily shrinks and is thus missed in a frozen section. In Fig. 8(g) and (h), the clusters of tumor regions are represented, and one of the clusters is segmented by a brown line as the cluster boundary. The use of all these biobank fresh tissue specimens was approved by the Institutional Review Board of Taipei Medical University (No. N202003041).

3.4. *Image validation: Comprehensive comparison between p-H&E and H&E-stained images of the same frozen-sectioned slice*

First, a dissected fresh metastatic SLN tissue with breast invasive ductal carcinoma (IDC) was prepared for frozen sectioning by surrounding it with cryostat gel (-20°C), and process II was followed, as shown in Fig. 4. Then, a 10- μ m-thick frozen-sectioned slice was affixed to the surface of a 1-mm-thick GS. Next, the GS-mounted slice was soaked by dropping PM #2 (containing 1.3% formaldehyde for better attachment) for 5 min, and the glass plate was slightly placed on this GS-mounted slice for further scanning and stitching p-H&E images. To stain this prefixed frozen slice, the glass plate was removed before H&E staining. Finally, the H&E-stained slice was sealed using mounting medium. Images acquired using p-H&E and H&E-stained methods for the same 10- μ m-thick frozen-sectioned slice are shown in Fig. 9(a) and 9(b), respectively.

Upon inspection of Fig. 9(a), the metastatic lesion in the SLN tissue could be readily identified in the light pink area of the lymphoid tissue. The same lesion in Fig. 9(b) appears purple. The micrometastatic lesion ($200\text{ }\mu\text{m} < \text{diameter} < 2\text{ mm}$) in the area enclosed by red lines can be observed in Fig. 9(c); a cluster of isolated tumor cells (ITCs; diameter $< 200\text{ }\mu\text{m}$, enclosed by green lines) is shown in Fig. 9(e). In Fig. 9(g), three single cancer cells are observed within a blood vessel (enclosed by blue lines). Figure 9(b) represents the co-localized H&E-stained image corresponding to the p-H&E image in Fig. 9(a). In Fig. 9(c) and 9(d), multiple clusters of IDC micrometastasis can be observed. In Fig. 9(e) and 9(f), cytoplasmic vacuolization, a characteristic feature of metastatic cancer, is evident. Comparing Fig. 9(g) with Fig. 9(h), single cancer cells in the tiny blood vessel surrounded by elastic fibers are resolved less clearly and are therefore more difficult to identify in the H&E-stained image.

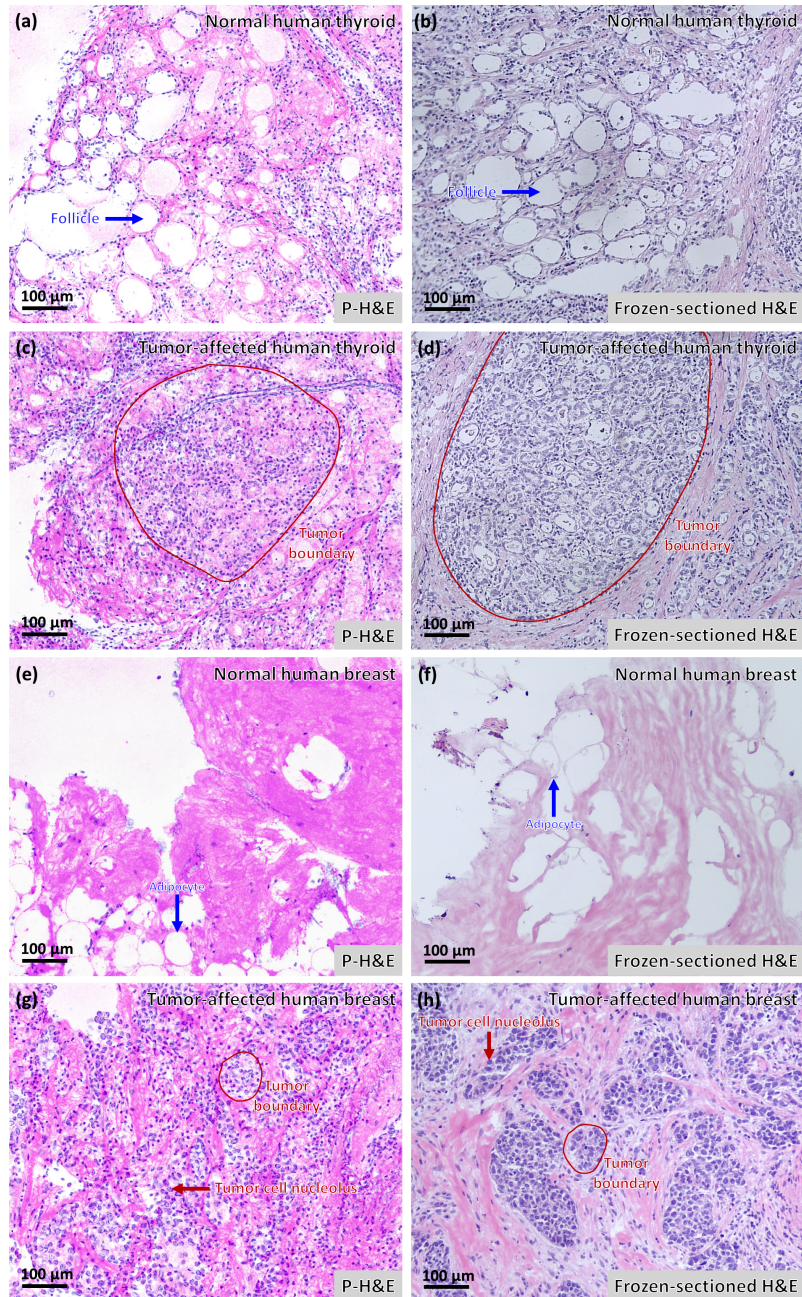


Fig. 8. Comparison of p-H&E and frozen-sectioned H&E images using the same fresh tissue pieces prior to warehouse entry of the biobank. Respectively, (a) and (c) show the p-H&E images of the normal and cancerous human thyroid tissue specimens at a scanning depth of 15 μm. (b) and (d) show both the frozen-sectioned H&E images obtained from the original tissue pieces of (a) and (c). Similarly, (e) and (g) separately show the p-H&E images of the normal and cancerous human breast tissue specimens at a scanning depth of 15 μm. (f) and (h) are the frozen-sectioned H&E images produced from the original tissue specimens of (e) and (g). For all figures, the FOV was 908 μm (W) × 736 μm (H).

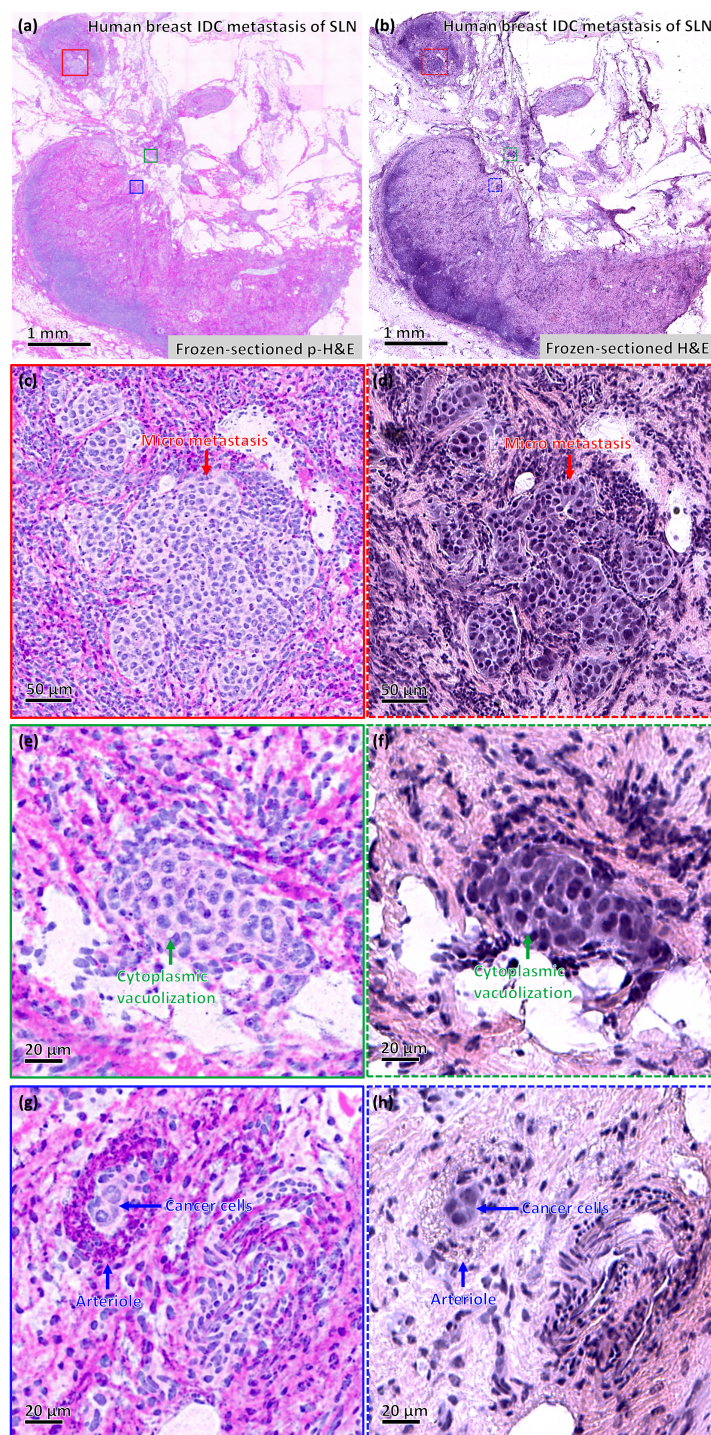


Fig. 9. (a) P-H&E and (b) H&E-stained images from the same 10- μ m-thick frozen-sectioned slice of fresh IDC-metastatic SLN tissue (each image covers the same 6.5 mm [W] \times 6.5 mm [H] area size). Images (c), (e), and (g) are magnified regions from (a), identified by the red, green, and blue boxes, respectively. Similarly, images (d), (f), and (h) are magnified regions from (b), identified by the red, green, and blue dashed boxes, respectively.

4. Discussion

Because of system dispersion resulting from optical components, measured axial and lateral resolutions of f-OCM are not as good as theoretical resolutions. In this system, the types of dispersion affecting resolution performance mainly come from optical component mismatch and incident angle dispersion. Optical component mismatch, resulted from unbalanced spectrums of reference and sample arms, will form worse autocorrelation FWHM of interferometric signal, so the axial resolution will become poor. Incident angle dispersion, resulted from using thick GPs and their thickness difference between reference and sample arms, will become poor especially when high NA objective is used, so the lateral resolution will become poor. But, based on the real submicron spatial resolution of f-OCM and LEDs properties, p-H&E images obtained using f-OCM were still able to exhibit high feature identification for cellular structures. LEDs used in f-OCM have the following properties: (1) a broadband near-Gaussian spectrum for OCM that prevents a ghost image, thus providing a high-quality cytoplasmic image [50]; (2) stable illumination intensity for FM that helps the p-H&E image to be unified and reproduced [51]; (3) long illumination lifetime that results in less light source replacement [52]; (4) small space requirement resulting in a compact imaging system [52]; and (5) cost-effectiveness [53]. Because this system utilizes visible-range broadband light, it could enable pigment-absorbed imaging of hemoglobin (in red blood cells) [54,55] and melanin (in melanocytes) [56], like adding orthogonal polarization spectral imaging [57] or sidestream dark field imaging [58] for additional colors of rapid H&E images.

In contrast to using separate cameras for FM and OCM, this f-OCM method combines co-localized functional and morphological features in a p-H&E image. In addition, the f-OCM system achieves co-localization by compensating the z-axial difference between coherent and focal planes. This can improve the positional correctness of morphological features for a p-H&E image in the scanned tissue specimen. In contrast to traditional *en-face* scans that rely on the movement of the reflector in the reference arm, this f-OCM system can eliminate the dust/scratches (on the reflector surface of the reference mirror) pattern from interference images generated using a four-step phase shifting algorithm through moving the z-axial piezoelectric stage incrementally because of no lateral movement of the reference mirror; this is particularly effective for a high-NA objective lens. In theory, the use of a higher NA objective lens [14] and SIM [31] can improve the axial resolution of FM considerably, further improving the nucleus quality of a p-H&E image. However, SIM can easily induce a grid line artifact after the calculation of background subtraction when the modulation speed of a Ronchi ruling is unstable.

Porcine tissues have become the general surgical model for both training and research globally because their anatomical and physiological characteristics [59] are similar to those of humans. In this study, eight types of normal fresh tissue samples of porcine organs, namely the cerebrum, kidney, lymph node, liver, skeletal muscle, salivary gland, lung, and esophagus, were scanned to produce several kinds of high-quality p-H&E images for the proposed system validation, where most cellular features could be easily observed for histological identification. This f-OCM system provided high resolution power for large-field p-H&E scans, which was sufficiently demonstrated by muscular striations and nucleus heterochromatins of the fresh porcine skeletal muscle. Thus, the porcine p-H&E images of neural axons in the cerebrum, Bowman's capsule and renal tubules in the kidney, high cell-density lymphocytes in lymph nodes, border-resolved hepatocytes in the liver, mucous and serous acini distinguishable in the salivary gland, complete contours of alveoli in the lungs, and squamous epithelium and lamina propria distinguished by a basal layer in the esophagus were all clearly represented.

In terms of biobank samples, two fresh thyroid and two fresh breast tissue specimens were scanned using the f-OCM system, processed as p-H&E images, and compared with their frozen-sectioned H&E-stained counterparts for the same original tissue pieces. In the two p-H&E images of thyroid tissue specimens, normal follicles and aggregate tumor cells could be easily identified.

For fresh breast tissue pieces, tumor clusters of the IDC specimen were easily identified compared with the normal ones because normal tissues have simple structures including collagen fibers, adipocytes, connective tissues, and breast ducts. The toxicity of PM #1 was low and exerted a negligible effect on cell culture *in vitro* (data not shown) because it has minor-groove binding ligands and lower membrane permeability. Currently, before warehouse storage in a biobank, tissue specimens are frozen-sectioned using the H&E method; however, the average yield rate is still low (~70%). With the low toxicity of PM and the high quality of p-H&E images, f-OCM scans can be useful for improving the tissue quality of fresh human tissue specimens before they are stored into the biobank. In addition, the typical size of fresh tissue specimens stored in a biobank is comparatively small when compared to intraoperative ones, thus requiring less time to scan; this is beneficial for the f-OCM system. In general, the total tissue processing time was less than 15 min before warehouse storage; thus, this system could effectively evaluate biobank tissue specimens.

To validate image similarity, we performed an in-depth comprehensive comparison between p-H&E and frozen-sectioned H&E images acquired from the same thick frozen-sectioned slices of fresh SLN tissue specimens that had been metastasized by an IDC. In general, the overall images of p-H&E and frozen-sectioned H&E images were quite similar. The key indicators of metastasis, including the presence of single cancer cells in a tiny blood vessel of the SNL, were resolved clearly in p-H&E images. Ultimately, p-H&E images revealed ultrastructural features in comparable details to traditional H&E-stained images. In addition, tiny blood vessel structures surrounded by elastic fibers and cytoplasmic vacuolization were clear in p-H&E images. The colors of p-H&E and H&E-stained images were not identical because this system used color space that was fine tuned by a previous default referring to paraffin-sectioned H&E images. Appropriate R, G, and B components to obtain high color similarity for frozen-sectioned H&E images were also available. Regarding the nuclei of cancer cells, some nucleoli were not represented in p-H&E images; these were identifiable in co-localized H&E-stained images because the RNA of nucleoli cannot be stained.

For rapid diagnosis using histopathology, the frozen-sectioned method is limited by many artifacts related to sample preparation (e.g., those resulting from fatty tissues and ice crystals). By contrast, our system, which uses Hoechst-stained fresh tissue specimens with 5-min soaking, provides high-quality p-H&E images at a depth of less than 50 μm beneath the surface of the attached fresh tissue specimen. The tissue-processing time of frozen-sectioned H&E slices starting from receiving the fatty or water-rich fresh tissue specimens is typically over 30 min on average. From a clinical perspective, compared with traditional frozen-sectioned H&E images, p-H&E images acquired using f-OCM could significantly shorten tissue-processing time to less than 15 min ($1 \times 1 \text{ cm}^2$) from receiving the fatty or water-rich fresh tissue specimens to delivering a pathological diagnosis. The tissue-processing time of the 1-cm^2 fresh tissue piece includes soaking the specimen (~5 min), attachment and autofocus of the specimen (<5 min), and scanning of the specimen (~4 min). Although the scan speed could be improved using a low magnification objective to increase the field of view, spatial resolution becomes poor.

5. Conclusion

Owing to its depth-scanning capability, the f-OCM system can capture continuous p-H&E images without any physical wastage of the tissue specimen. In total, the processing time from receiving an approximately 1-cm^2 fresh tissue specimen for scanning to generating the entire *en-face* p-H&E image was less than 15 min, which is two times faster than the time required for the typical frozen-sectioned H&E process for fatty or water-rich tissue specimens on average. In contrast to digital H&E visualization, image data generated by two independent optical sectioning methods provide more in-depth information that can be used to observe additional morphological features of individual gray-level channels [60], and the data can be used to train AI-based image

segmentation methods to distinguish cancer tissues from normal tissues [61]. In short, the p-H&E imaging technique has high applicability for histopathology (including intraoperative histology and biopsies for brain and breast tumor diagnoses) and offers a viable alternative to the frozen-sectioning method. This method may assist veterinary and human surgeons in surgery-related treatment planning. In addition, digital p-H&E imaging can be used to realize telepathology in the field of rapid image diagnosis.

Acknowledgments. We acknowledge the contribution of the Joint Biobank, Office of Human Research, Taipei Medical University (TMU), who supplied the biobank block tissues and assisted with the IRB approval of N202003041.

Disclosures. The authors declare no conflicts of interest related to this article.

Data availability. Data underlying the results presented in this paper are not publicly available at this time but may be obtained from the authors upon reasonable request.

References

1. J. C. Wyant, "White light extended source shearing interferometer," *Appl. Opt.* **13**(1), 200–203 (1974).
2. A. F. Fercher, K. Mengedocht, and W. Werner, "Eye-length measurement by interferometry with partially coherent light," *Opt. Lett.* **13**(3), 186–188 (1988).
3. D. Huang, E. A. Swanson, C. P. Lin, J. S. Schuman, W. G. Stinson, W. Chang, M. R. Hee, T. Flotte, K. Gregory, C. A. Puliafito, and J. G. Fujimoto, "Optical coherence tomography," *Science* **254**(5035), 1178–1181 (1991).
4. A. F. Fercher, C. K. Hitzenberger, G. Kamp, and S. Y. El-Zaiat, "Measurement of intraocular distances by backscattering spectral interferometry," *Opt. Commun.* **117**(1-2), 43–48 (1995).
5. J. Wang, Y. Xu, and S. A. Boppart, "Review of optical coherence tomography in oncology," *J. Biomed. Opt.* **22**(12), 121711 (2017).
6. I. E. Tampu, M. Maintz, D. Koller, K. Johansson, O. Gimm, A. Capitanio, A. Eklund, and N. Haj-Hosseini, "Optical coherence tomography for thyroid pathology: 3D analysis of tissue microstructure," *Biomed. Opt. Express* **11**(8), 4130–4149 (2020).
7. A. Dubois, K. Grieve, G. Moneron, R. Lecaue, L. Vabre, and C. Boccara, "Ultrahigh-resolution full-field optical coherence tomography," *Appl. Opt.* **43**(14), 2874–2883 (2004).
8. E. Beaurepaire, A. C. Boccara, M. Lebec, L. Blanchot, and H. Saint-Jalmes, "Full-field optical coherence microscope," *Opt. Lett.* **23**(4), 244–246 (1998).
9. L. Vabre, A. Dubois, and A. C. Boccara, "Thermal-light full-field optical coherence tomography," *Opt. Lett.* **27**(7), 530–532 (2002).
10. J. G. Zheng, D. Lu, T. Chen, C. Wang, N. Tian, F. Zhao, T. Huo, N. Zhang, D. Chen, W. Ma, J. L. Sun, and P. Xue, "Label-free subcellular 3D live imaging of preimplantation mouse embryos with full-field optical coherence tomography," *J. Biomed. Opt.* **17**(7), 1 (2012).
11. W. J. Choi, K. S. Park, T. J. Eom, M.-K. Oh, and B. H. Lee, "Tomographic imaging of a suspending single live cell using optical tweezer-combined full-field optical coherence tomography," *Opt. Lett.* **37**(14), 2784–2786 (2012).
12. M. Jain, N. Shukla, M. Manzoor, S. Nadolny, and S. Mukherjee, "Modified full-field optical coherence tomography: A novel tool for rapid histology of tissues," *J Pathol Inform* **2**(1), 28 (2011).
13. O. Assayag, M. Antoine, B. Sigal-Zafrani, M. Riben, F. Harms, A. Burcheri, K. Grieve, E. Dalimier, B. L. C. de Poly, and C. Boccara, "Large field, high resolution full-field optical coherence tomography: a pre-clinical study of human breast tissue and cancer assessment," *TCRT Express* **13**(5), 455–468 (2014).
14. M. Jain, N. Narula, B. Salamoan, M. M. Shevchuk, A. Aggarwal, N. Altorki, B. Stiles, C. Boccara, and S. Mukherjee, "Full-field optical coherence tomography for the analysis of fresh unstained human lobectomy specimens," *J Pathol Inform* **4**(1), 26 (2013).
15. C. Apelian, F. Harms, O. Thouvenin, and A. C. Boccara, "Dynamic full field optical coherence tomography: subcellular metabolic contrast revealed in tissues by interferometric signals temporal analysis," *Biomed. Opt. Express* **7**(4), 1511–1524 (2016).
16. H. Yang, S. Zhang, P. Liu, L. Cheng, F. Tong, H. Liu, S. Wang, M. Liu, C. Wang, Y. Peng, F. Xie, B. Zhou, Y. Cao, J. Guo, Y. Zhang, Y. Ma, D. Shen, P. Xi, and S. Wang, "Use of high-resolution full-field optical coherence tomography and dynamic cell imaging for rapid intraoperative diagnosis during breast cancer surgery," *Cancer* **126**(S16), 3847–3856 (2020).
17. O. Thouvenin, C. Apelian, A. Nahas, M. Fink, and C. Boccara, "Full-Field Optical Coherence Tomography as a Diagnosis Tool: Recent Progress with Multimodal Imaging," *Appl. Sci.* **7**(3), 236 (2017).
18. C. C. Tsai, C. K. Chang, K. Y. Hsu, T. S. Ho, M. Y. Lin, J. W. Tjiu, and S. L. Huang, "Full-depth epidermis tomography using a Mirau-based full-field optical coherence tomography," *Biomed. Opt. Express* **5**(9), 3001–3010 (2014).
19. A. Federici and A. Dubois, "Full-field optical coherence microscopy with optimized ultrahigh spatial resolution," *Opt. Lett.* **40**(22), 5347–5350 (2015).
20. J. Pérez-Anker, J. Malvehy, and D. Moreno-Ramírez, "Ex Vivo Confocal Microscopy Using Fusion Mode and Digital Staining: Changing Paradigms in Histological Diagnosis," *Actas Dermosifiliogr.* **111**(3), 236–242 (2020).

21. M. Ragazzi, S. Piana, C. Longo, F. Castagnetti, M. Foroni, G. Ferrari, G. Gardini, and G. Pellacani, "Fluorescence confocal microscopy for pathologists," *Mod. Pathol.* **27**(3), 460–471 (2014).
22. S. Yuan, C. A. Roney, y. Wierwillel, C. W. Chen, B. Xu, G. Griffiths, J. Jiang, H. Ma, A. Cable, R. M. Summers, and Y. Chen, "Co-registered optical coherence tomography and fluorescence molecular imaging for simultaneous morphological and molecular imaging," *Phys. Med. Biol.* **55**(1), 191–206 (2010).
23. E. Aukorius, Y. Bromberg, R. Motiejūnaitė, A. Pieretti, L. Liu, E. Coron, J. Aranda, A. M. Goldstein, B. E. Bouma, A. Kazlauskas, and G. J. Tearney, "Dual-modality fluorescence and full-field optical coherence microscopy for biomedical imaging applications," *Biomed. Opt. Express* **3**(3), 661–666 (2012).
24. F. Harms, B. de Poly, and A. C. Boccara, "Multimodal full-field optical coherence tomography on biological tissue: toward all optical digital pathology," *Proc. SPIE* **8216**, 821609 (2012).
25. D. S. Gareau, "The feasibility of digital stained multimodal confocal mosaics to simulate histopathology," *J. Biomed. Opt.* **14**(3), 034050 (2009).
26. V. A. Byvaltsev, L. A. Bardanova, N. R. Onaka, R. A. Polkin, S. V. Ochkal, V. V. Shepelev, M. A. Aliyev, and A. A. Potapov, "Acridine orange: a review of novel applications for surgical cancer imaging and therapy," *Front. Oncol.* **9**, 925 (2019).
27. Y. K. Tao, D. Shen, Y. Sheikine, O. O. Ahsen, H. H. Wang, D. B. Schmolze, N. B. Johnson, J. S. Brooker, A. E. Cable, J. L. Connolly, and J. G. Fujimoto, "Assessment of breast pathologies using nonlinear microscopy," *Proceedings of the National Academy of Sciences* **111**(43), 15304–15309 (2014).
28. L. C. Cahill, M. G. Giacomelli, T. Yoshitake, H. Vardeh, B. E. Faulkner-Jones, J. L. Connolly, C. K. Sun, and James G Fujimoto, "Rapid virtual hematoxylin and eosin histology of breast tissue specimens using a compact fluorescence nonlinear microscope," *Lab. Invest.* **98**(1), 150–160 (2018).
29. D. A. Orringer, B. Pandian, Y. S. Niknafs, T. C. Hollon, J. Boyle, S. Lewis, M. Garrard, S. L. Hervey-Jumper, H. J. L. Garton, C. O. Maher, J. A. Heth, O. Sagher, D. A. Wilkinson, M. Snuderl, S. Venneti, S. H. Ramkissoon, K. A. McFadden, A. Fisher-Hubbard, A. P. Lieberman, T. D. Johnson, X. S. Xie, J. K. Trautman, C. W. Freudiger, and S. Camelo-Piragua, "Rapid intraoperative histology of unprocessed surgical specimens via fibre-laser-based stimulated Raman scattering microscopy," *Nat. Biomed. Eng.* **1**(2), 0027 (2017).
30. T. C. Hollon and D. A. Orringer, "An automated tissue-to-diagnosis pipeline using intraoperative stimulated Raman histology and deep learning," *Molecular & Cellular Oncology* **7**(3), 1736742 (2020).
31. K. N. Elfer, A. B. Sholl, M. Wang, D. B. Tulman, S. H. Mandava, B. R. Lee, and J. Q. Brown, "DRAQ5 and eosin ('D&E') as an analog to hematoxylin and eosin for rapid fluorescence histology of fresh tissues," *PLoS ONE* **11**(10), e0165530 (2016).
32. W. Xie, Y. Chen, Y. Wang, L. Wei, C. Yin, A. K. Glaser, M. E. Fauver, E. J. Seibel, S. M. Dintzis, J. C. Vaughan, N. P. Reder, and J. T. C. Liu, "Microscopy with ultraviolet surface excitation for wide-area pathology of breast surgical margins," *J. Biomed. Opt.* **24**(2), 026501 (2019).
33. T. Yoshitake, M. G. Giacomelli, L. M. Quintana, H. Vardeh, L. C. Cahill, B. E. Faulkner-Jones, J. L. Connolly, D. Do, and J. G. Fujimoto, "Rapid histopathological imaging of skin and breast cancer surgical specimens using immersion microscopy with ultraviolet surface excitation," *Sci. Rep.* **8**(1), 4476 (2018).
34. Y. Chen, W. Xie, A. K. Glaser, N. P. Reder, C. Mao, S. M. Dintzis, J. C. Vaughan, and J. T. C. Liu, "Rapid pathology of lumpectomy margins with open-top light-sheet (OTLS) microscopy," *Biomed. Opt. Express* **10**(3), 1257–1272 (2019).
35. S. Krishnamurthy, J. Q. Brown, N. Iftimia, R. M. Levenson, and M. Rajadhyaksha, "Ex vivo microscopy: a promising next-generation digital microscopy tool for surgical pathology practice," *Lab. Invest.* **143**(9), 1058–1068 (2019).
36. C. C. Tsai and K. Y. Hsu, "Optical sectioning apparatus using advanced optical interference microscopy," U.S. patent 10,151,572B1 (11 December 2018).
37. C. C. Tsai, K. Y. Hsu, D. Y. Jheng, and S. E. Lin, "Pseudo H and E image producing method and optical system using same," U.S. patent 10,665,000B2 (26 May 2020).
38. E. Ciarrocchi and N. Belcari, "Cerenkov luminescence imaging: physics principles and potential applications in biomedical sciences," *EJNMMI Phys* **4**(1), 14 (2017).
39. S. R. Sternberg, "Biomedical Image Processing," *Computer* **16**(1), 22–34 (1983).
40. W. Zhang, H. He, L. Gong, W. Lai, B. Dong, and L. Zhang, "Effects of sweetener sucralose on diet preference, growth performance and hematological and biochemical parameters of weaned piglets," *Asian-Australas J Anim Sci* **33**(5), 802–811 (2020).
41. A. Kalita, P. C. Kalita, and P. J. Doley, "Light microscopic study on the peripheral lymphnodes of Mizo local pig (Zo Vawk)," *Asian j. biomed. pharm.* **4**(28), 7–12 (2014).
42. S. R. Yinti, S. Natarajan, K. Boaz, A. J. Lewis, J. Pandya, and S. N. Kapila, "Analysis of reticulin fiber pattern in lymph nodes with metastasis from oral squamous cell carcinoma," *Dent. Hypotheses* **6**(3), 104–108 (2016).
43. S. H. Mirmalek-Sani, D. C. Sullivan, C. Zimmerman, T. D. Shupe, and B. E. Petersen, "Immunogenicity of decellularized porcine liver for bioengineered hepatic tissue," *Am. J. Pathol.* **183**(2), 558–565 (2013).
44. P. L. Powell, R. R. Roy, P. Kanim, M. A. Bello, and V. R. Edgerton, "Predictability of skeletal muscle tension from architectural determinations in guinea pig hindlimbs," *Journal of Applied Physiology* **57**(6), 1715–1721 (1984).
45. C. Boudoux, S. H. Yun, W. Y. Oh, W. M. White, N. V. Iftimia, M. Shishkov, B. E. Bouma, and G. J. Tearney, "Rapid wavelength-swept spectrally encoded confocal microscopy," *Opt. Express* **13**(20), 8214–8221 (2005).

46. Q. Sun, Y. Li, S. He, C. Situ, Z. Wu, and J. Y. Qu, "Label-free multimodal nonlinear optical microscopy reveals fundamental insights of skeletal muscle development," *Biomed. Opt. Express* **5**(1), 158–166 (2014).
47. G. Urkasemsin, P. Castillo, S. Rungarunlert, N. Klincumhom, and J. N. Ferreira, "Strategies for developing functional secretory epithelia from porcine salivary gland explant outgrowth culture models," *Biomolecules* **9**(11), 657 (2019).
48. F. Harrison, A. Muruli, S. Higgins, and S. P. Diggle, "Development of an *ex vivo* porcine lung model for studying growth, virulence, and signaling of *Pseudomonas aeruginosa*," *Infect. Immun.* **82**(8), 3312–3323 (2014).
49. R. J. von Furstenberg, J. Li, C. Stolarchuk, R. Feder, A. Campbell, L. Kruger, L. M. Gonzalez, A. T. Blikslager, D. M. Cardona, S. J. McCall, S. J. Henning, and K. S. Garman, "Porcine esophageal submucosal gland culture model shows capacity for proliferation and differentiation," *Cellular and Molecular Gastroenterology and Hepatology* **4**(3), 385–404 (2017).
50. C. C. Tsai, T. H. Chen, Y. S. Lin, Y. T. Wang, W. Chang, K. Y. Hsu, Y. H. Chang, P. K. Hsu, D. Y. Jheng, K. Y. Huang, E. Sun, and S. L. Huang, "Ce³⁺:YAG double-clad crystal-fiber-based optical coherence tomography on fish cornea," *Opt. Lett.* **35**(6), 811–813 (2010).
51. F. Mubaid, D. Kaufman, T. L. Wee, D. S. Nguyen-Huu, D. Young, M. Anghelopoulou, and C. M Brown, "Fluorescence microscope light source stability," *Histochem. Cell Biol.* **151**(4), 357–366 (2019).
52. J. Ogien and A. Dubois, "High-resolution full-field optical coherence microscopy using a broadband light-emitting diode," *Biomed. Opt. Express* **24**(9), 9922–9931 (2016).
53. T. Anna, T. W. Chang, C. M. Lai, A. Chiou, and W. C. Kuo, "A Feasibility Study of Broadband White Light Emitting Diode (WLED) based Full-Field Optical Coherence Microscopy (FF-OCM) using Derivative-based Algorithm," *IEEE Photonics J.* **9**(2), 1–13 (2017).
54. F. E. Robles, S. Chowdhury, and A. Wax, "Assessing hemoglobin concentration using spectroscopic optical coherence tomography for feasibility of tissue diagnostics," *Biomed. Opt. Express* **1**(1), 310–317 (2010).
55. X. Shu, L. J. Beckmann, and H. F. Zhang, "Visible-light optical coherence tomography: a review," *J. Biomed. Opt.* **22**(12), 121707 (2017).
56. D. J Harper, T. Konegger, M. Augustin, K. Schützenberger, P. Eugui, A. Lichtenegger, C. W. Merkle, C. K. Hitznerberger, M. Glösmann, and B. Baumann, "Hyperspectral optical coherence tomography for in vivo visualization of melanin in the retinal pigment epithelium," *J. Biophotonics* **12**(12), e201900153 (2019).
57. W. Groner, J. W. Winkelman, A. G. Harris, C. Ince, G. J. Bouma, K. Messmer, and R. G. Nadeau, "Orthogonal polarization spectral imaging: A new method for study of the microcirculation," *Nat. Med.* **5**(10), 1209–1212 (1999).
58. P. T. Goedhart, M. Khalilzada, R. Bezemer, J. Merza, and C. Ince, "Sidestream Dark Field (SDF) imaging: a novel stroboscopic LED ring-based imaging modality for clinical assessment of the microcirculation," *Opt. Express* **15**(23), 15101–15114 (2007).
59. M. M. Swindle, A. Makin, A. J. Herron, F. J. Clubb Jr, and K. S. Frazier, "Swine as models in biomedical research and toxicology testing," *Vet. Pathol.* **49**(2), 344–356 (2012).
60. N. Sladoje and J. Lindblad, "High-precision boundary length estimation by utilizing gray-level information," *IEEE Trans. Pattern Anal. Mach. Intell.* **31**(2), 357–363 (2009).
61. M. Gavrilovic, J. C. Azar, J. Lindblad, C. Wählby, E. Bengtsson, C. Busch, and I. B. Carlbom, "Blind color decomposition of histological images," *IEEE Trans. Med. Imag.* **32**(6), 983–994 (2013).